Results in Physics 11 (2018) 85–95

Contents lists available at ScienceDirect

Results in Physics

journal homepage: www.elsevier.com/locate/rinp

Harnessing 3D printed residual stress to design heat-shrinkable metamaterials

Yangbo Li[a,*], Siyu Cao[a], Tiantian Li[b], Lifeng Wang[b,*]

[a] College of Hydraulic and Environmental Engineering, China Three Gorges University, Yichang, Hubei 443002, China
[b] Department of Mechanical Engineering, State University of New York at Stony Brook, Stony Brook, NY 11794, USA

ARTICLE INFO

Keywords:
Residual stress
Metamaterial
Lattice
Heat-shrinkable
Photochemical expansion

ABSTRACT

Heat-shrinkable materials, which are typically shape-memory polymers and irreversibly shrink in response to external heating stimuli, are vital for coating and protection applications in aerospace, micro-robotics, biomedical devices, and biomimetic systems. In these applications, they are often subjected to complex environmental conditions, such as thermal and mechanical loading, which induce a certain level of deformation. It is imperative to understand the resultant deformation and internal stress state under these loading conditions. Here we report a new class of heat-shrinkable metamaterials, which utilize photochemical expansion in 3D printing to release locally residual stress with the heat-shrinkage rate of 3–8%. Planar lattice metamaterials are designed to evolve into permanent heat-shrinkage status. The fundamental mechanisms that control heat-shrinkable behavior are identified and tested in thermal experiments. The photochemical expansion strain rises with the increase of layer printing time and nozzle proceeding direction. Furthermore, analytical predictions agree well with the experiments about the unrecoverable heat-shrinkable strain and the recoverable thermal strain of the proposed unit cell. The findings presented here enable heat-shrinkable metamaterials with simple fabrication and porosity, dramatically reducing required manufacture times and materials.

Introduction

Heat-shrinkable materials [1,2] are a class of materials having the capability to change their shapes or state from temporary to permanent in response to thermal stimuli. They can keep the permanent shrinkage state in the normal temperature. Compared to materials with negative thermal expansion [3–6], the heat-shrinkable materials irreversibly shrink when heated. This unique property makes them widely employed for coating and packaging in such engineering applications as self-deploying sun-sails or antenna, morphing wing structures, packaging or wrinkle-free fabrics [7–9]. Shape-memory polymers (SMPs) is one of them [10]. The SMPs are also used as raw materials in 3D printing, a stereolithography rapid prototyping process that supervene real-time thermo-mechanical mismatches between constituents, or the product and the tray. Typically, mismatches inevitably cause residual stresses, as well as consequent errors and failures such as geometric imperfection or distortion [11,12] in the metallic additive manufacturing [13–15], concrete dams, and bridges [16]. To diminish residual thermal stresses in these engineering structures, numerous measurements have been taken into consideration such as pipe-cooling concrete, slicing to dam sections and grouting into integration, or post-thermal-process, which need tremendous extra cost [17]. Therefore, how to harness residual stress is of great concern among scientists and engineers. The successful explorations have been done in polymeric four-dimensional (4D) printing [18–23], plants blossoming [24,25] by creating versatile morphology [26] for the applications such as micro-robotics [27], biomedical devices [28], and biomimetic systems [29].

Inspired by recent advances in four-dimensional (4D) printing, we uncover that residual stresses in 3D printing can be harnessed to design heat-shrinkable metamaterials. Compared with conventional heat-shrinkable materials, the proposed heat-shrinkable metamaterials can be readily fabricated by commercial 3D printers and the pre-heating step can be omitted in the production process. Furthermore, because of their porosity, they consume less material than conventional ones. Those advantages will make heat-shrinkable metamaterials gradually replacing the conventional materials for packaging, coating, sealing, shielding and protection in such industries as food, chemistry, petroleum pipeline, household appliance, cables, and defense communication, etc. Meanwhile, prior research has thoroughly investigated that shrinkage of stereolithography photo-curable resins, including the elastomer (Tangoplus) and the glassy polymer (Verowhite), under ultraviolet and thermal exposure [26,30,31].

* Corresponding authors.
E-mail addresses: liyangbo@ctgu.edu.cn (Y. Li), lifeng.wang@stonybrook.edu (L. Wang).

https://doi.org/10.1016/j.rinp.2018.08.034
Received 18 July 2018; Received in revised form 16 August 2018; Accepted 16 August 2018
Available online 25 August 2018

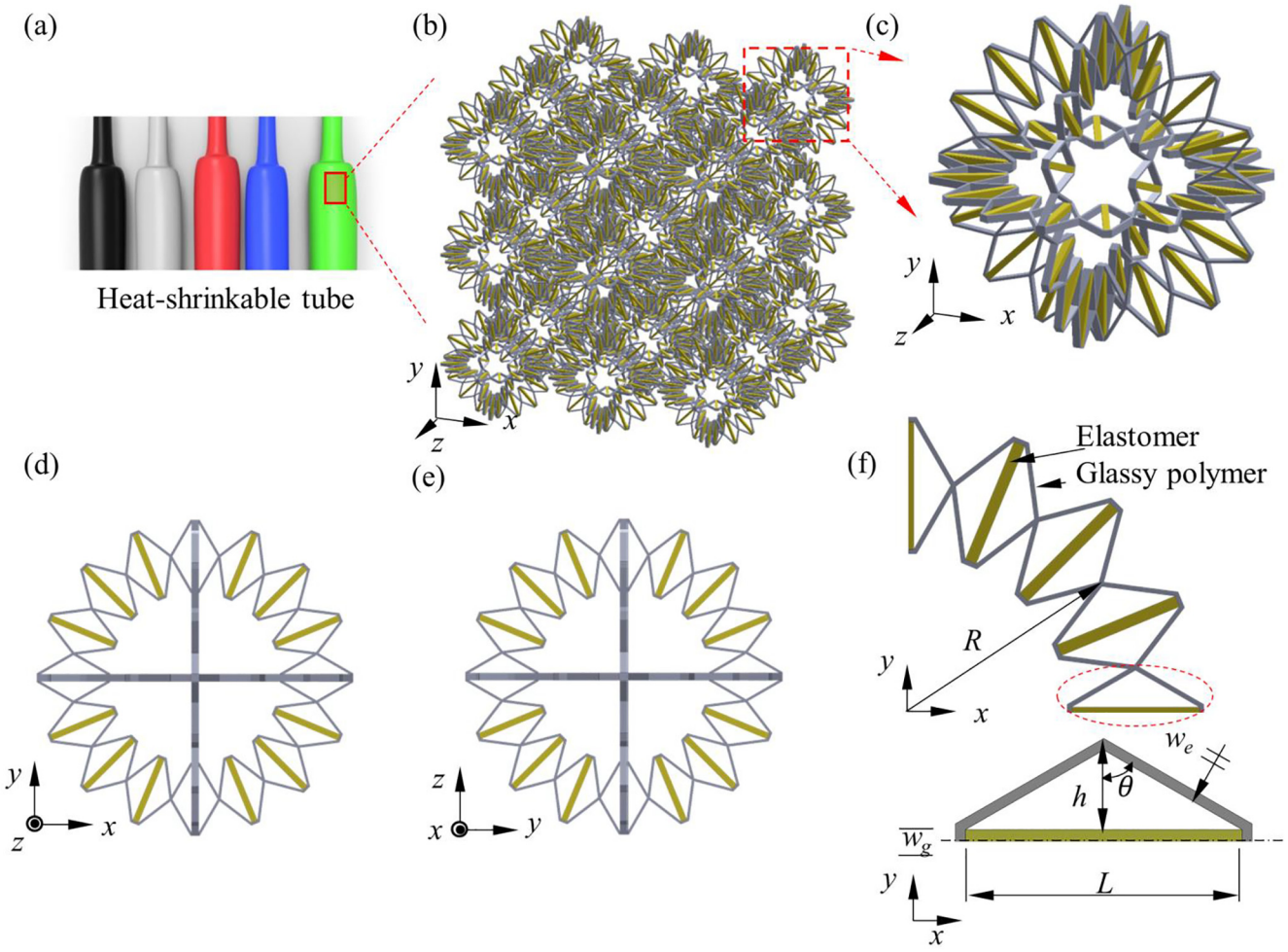

Fig. 1. Schematics of the proposed heat-shrinkable metamaterial. (a) The heat-shrinkable tubes, (b) the schematic of the proposed 3D metamaterial, consisting of $3 \times 3 \times 3$ unit cells in x, y, and z coordinates, (c) a 3D unit cell, (d) the top, and (e) front view of a unit cell as well as (f) the composition of a quarter unit cell along with a half diamond element in a unit cell.

Here, we design a class of bi-material lattice metamaterials and fabricated the specimens using a commercial 3D printer. The thermo-mechanical response of the proposed metamaterials including the permanent shrinkage rate is experimentally investigated. Moreover, we examine the occurrence of the photochemical expansion during the 3D printing process due to the built-in compressive strain, which is enabled by tailoring the layer printing time and the 3D printing direction. Finally, based on the direct stiffness method of the beams system, quantitatively analytical predictions considering microstructure topology and built-in compressive strain are conducted to verify the experiments and understand the source of heat shrinkage and the mechanism of permanent shrinkage.

Materials and methods

Metamaterials design

To achieve the irreversible shrinkage by virtue of 3D printing technology, we propose a methodology to develop 3D heat-shrinkable metamaterials in Fig. 1(a) and 1(b), which are combined with repeated 3D unit cells (Fig. 1(c)) by a simple cubic lattice symmetry in the microscopic scale. In the Cartesian coordinate system, three mutually perpendicular equal planar unit cells as shown in Fig. 1(d)–(e) share a common center and are assembled into a 3D unit cell. Intuitively, the volumetric change in the 3D unit cell in Fig. 1(c) induces expansion or shrinkage in the heat-shrinkable tube in Fig. 1(a). Due to the mutually perpendicular distribution of three equal planar unit cells, the planar unit cell determines the response of the 3D metamaterials. For simplicity, we perform the analysis of the planar unit cell to represent the 3D metamaterials in this work.

In the planar unit cell, we continue to abstract a fundamental element – the diamond shown in Fig. 1(f), which is composed of a glassy polymer rhombus and an elastomer beam. A number of equal diamond elements evenly distributed along with a center consisting of a planar unit cell as shown in Fig. 1(f), where n is the number of half-diamond triangle elements, and θ_0 the half vertex angle of the triangle, and R the radius of the diamond circle. When the angle θ_0 in the diamond is infinitely close to 90°, the circumference of the planar unit cell will become a minimum value. Simultaneously, the length L will be close to maximum value. Therefore, when the elastomer beam becomes longer, the planar unit cell will shrink. Once there is a way that makes the elastomer beam permanently longer than ever, the proposed metamaterials will keep a permanently shrinking state. If they are used to replace the traditional heat-shrinkable materials, their porosity will make them tremendously economic materials. Although the hinge in the current unit cell design could be the potential failure point, we may strengthen locally those hinges by thickening those points to avoid the potential failure.

Experiments

To investigate the possible heat shrinkage of the proposed

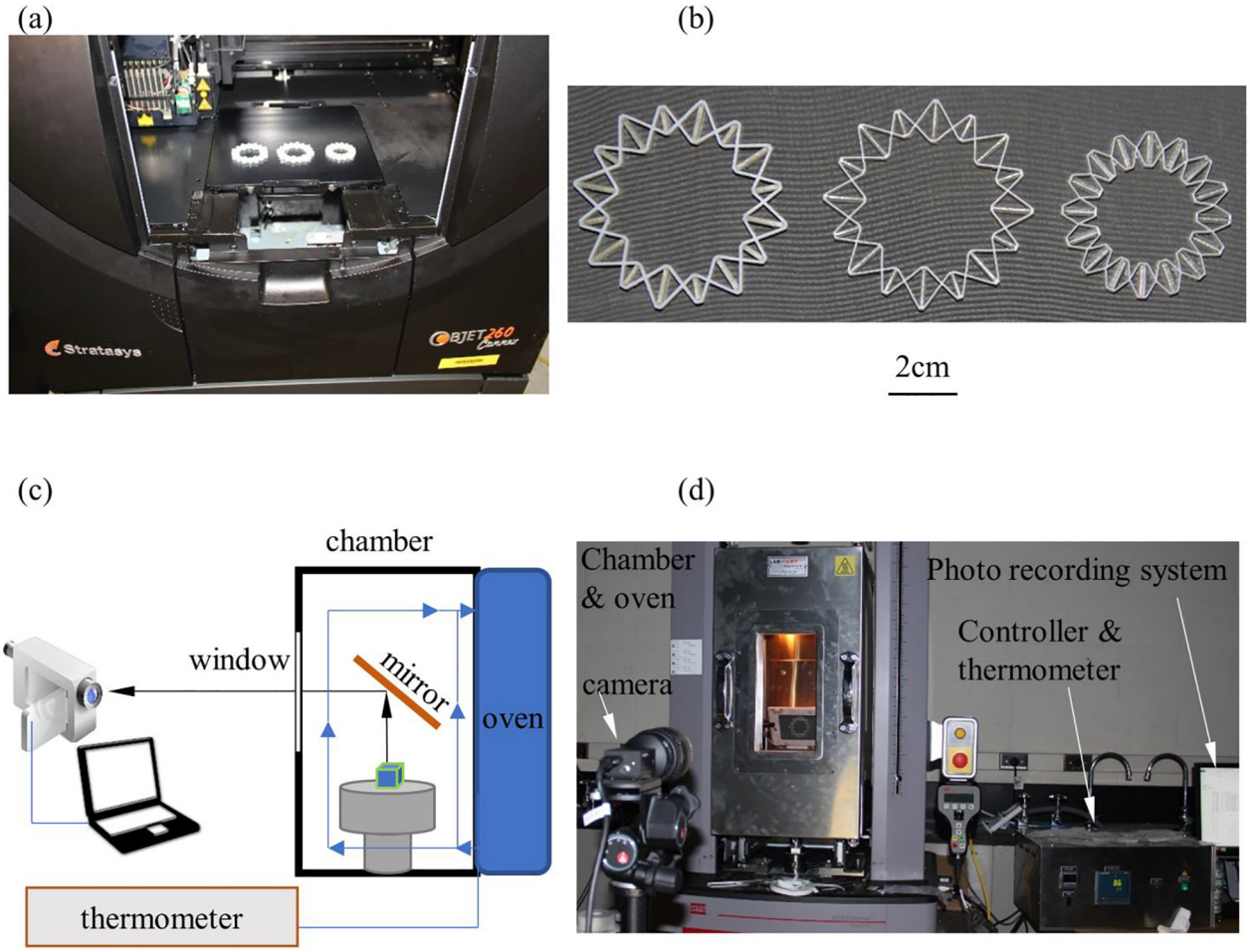

Fig. 2. 3D printed fabrication and experimental set-up. (a) Fabrication process, (b) specimens, (c) schematic experimental set-up, and (d) the real set-up of the experiment. The hot air in the oven is blown into the chamber from the bottom outlet, while the relatively cold air in the chamber is drawn into the oven through the top inlet, which constitutes a heating recycle. The specimen placed on the gray tray is projected into the lens of the camera by the mirror, which is used to avoid deformation from its own gravity.

metamaterials, we fabricated the specimens and designed the experimental setup to measure their thermomechanical response by the thermal stimulus, as shown in Fig. 2. The experimental setup consists of a high-speed camera and photo recording system in the computer (POINT GREY), chamber and oven (Lab-Temp by ThermCraft), and temperature controller and thermometer. The hot air in the oven is blown into the chamber from the bottom outlet, while the relatively cold air in the chamber is drawn into the oven through the top inlet, which constitutes a heating cycle. The high-speed camera focuses on the specimen placed horizontally on the tray in the oven by the mirror reflection, capturing the shape evolution with the temperature increase at the second rate. Here, we used the mirror to avoid the effect of the sample's own gravity.

The proposed metamaterials agree with the macro-scale planar unit cell in the thermally deformed mechanism. So, the planar unit cells with $w_e = 0.2\,\text{mm}$, $w_g = 0.5\,\text{mm}$, $\theta_0 = 60^\circ$, $R_0 = 10\,\text{mm}$, and $n = 32$ are used as the analysis object. The specimens of planar unit cells were fabricated by using a multi-material 3D printer (Connex Objet260). TangoPlus was used as the elastomer (Young's Modulus $E_h = 5.5\,\text{MPa}$), and VeroWhite was used as the glassy polymer (Young's Modulus $E_l = 1600\,\text{MPa}$).The thermal deformation measurement of these two constituent materials was conducted and the results were shown in Fig. A1 (Appendix). The coefficients of thermal expansion for VeroWhite and TangoPlus can be calculated as $1.64 \times 10^{-4}\,^\circ\text{C}^{-1}$ and $3.0 \times 10^{-4}\,^\circ\text{C}^{-1}$, respectively. Both of their Poission's Ratios are 0.3. The samples of proposed metamaterials were placed in a chamber where the temperature was slowly increased from 22.4 °C to 68.1 °C.

Results and discussion

Heat shrinkage

In Fig. 3(a)–(b), we exhibit the images of the samples before and after heating. Here, the red thin outlines represent the projected area of the samples at room temperature. It is noticed that the sample with metamaterial structures considerably shrinks homogenously toward the center of the specimen (Fig. 3(b)) after the temperature increases. To quantitatively capture the thermal shrinkage, we calculate the strain along with x and y-directions as $\varepsilon_x = \varepsilon_y = \frac{A - A_0}{2A_0}$, where A and A_0 denote the outline area of the specimen at the heating temperatures and the room temperature of 22.4 °C, respectively. We find that the shrinkage strain reaches 2.8% in both directions when the temperature increases from 22.4 °C to 68.1 °C.

In order to find the source of heat shrinkage of the planar unit cell, we simulated its deformation using the finite element tool ABAQUS with a quarter of the unit cell and considering the photochemical expansion in the middle elastomer beams (Fig. 3(c)) and thermal expansion coefficients of two constituents (Fig. 3(d)), respectively. In our simulations, we consider a quarter of a unit cell with suitable periodic boundary conditions. Detailedly, all the nodes on the x-axis are constrained as $y = 0$ (displacement of y-direction), all the nodes on the y-axis $x = 0$ (displacement of x-direction) as shown in Fig. 3(c) and (d).

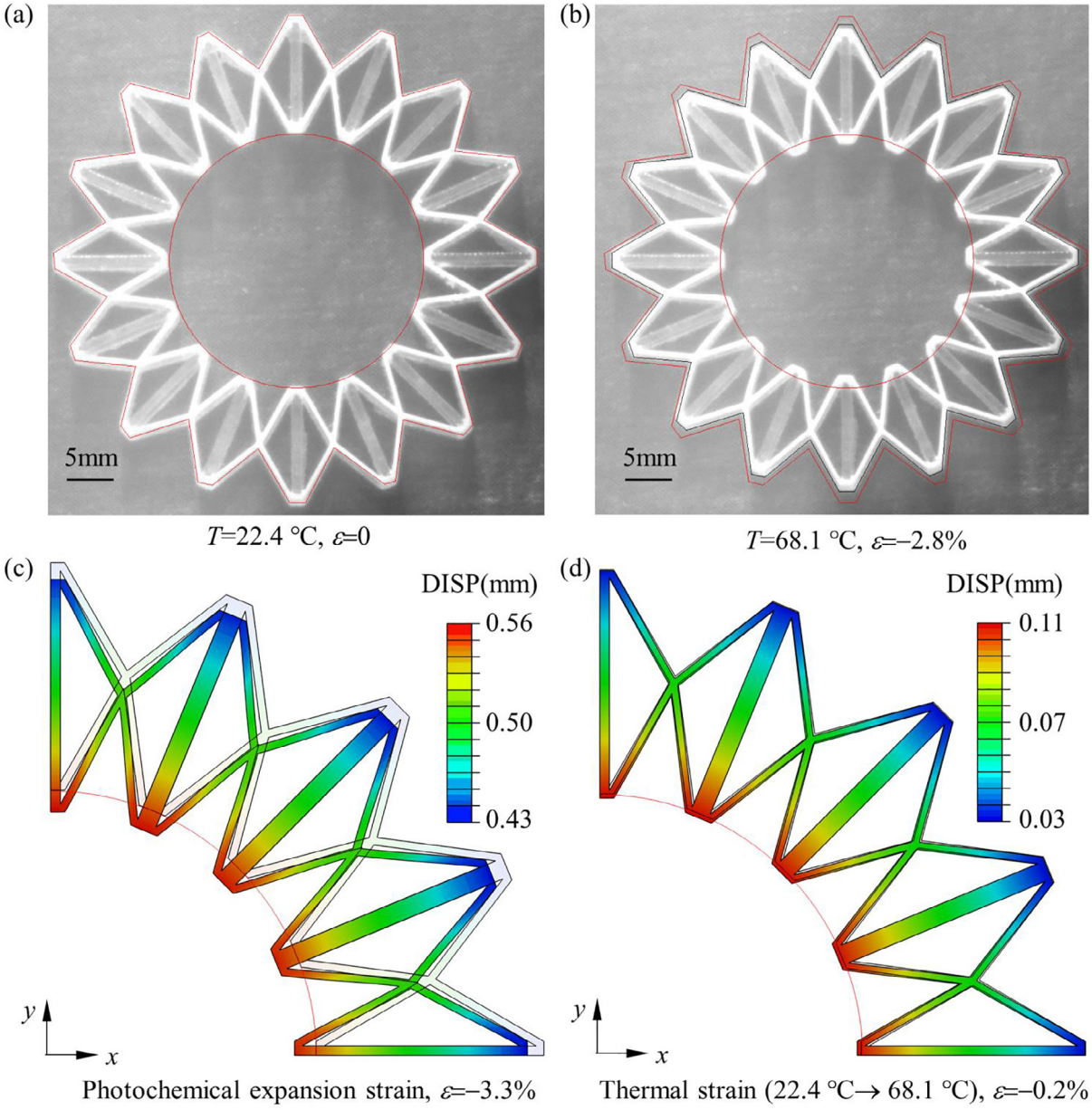

Fig. 3. Experimental and numerical results of a planar unit cell with temperature increase from 22.4 °C to 68.1 °C. Experimental snapshots record the deformation of the samples at the temperature of (a) 22.4 °C and (b) 68.1 °C. The deformation contour (c) indicates the displacement field of the planar unit cell when the photochemical expansion (2.2%) in the middle elastomer beams is only considered. The deformation contour (d) shows the displacement field of the planar unit cell when thermal expansion coefficients of two constituents are only considered from 22.4 °C to 68.1 °C.

2D solid models are constructed using 4-node bilinear plain stress element CPS4R, which is based on the plain stress assumption. No out-of-plane deformation is included in the current study. The photochemical expansion (2.2%) in the middle elastomer beams is considered in Fig. 3(c), while thermal load is considered for the temperature change from the 22.4 °C to 68.1 °C, both of which keep coincide with the experimental loads. The geometrical and mechanical parameters of the unit cells are same as the experiment. The comparison between Fig. 3(b), (c), and (d) implies that 2.8% of the strain in the experiment may derive from photochemical expansion in the elastomer beams other than the thermal expansion coefficients of two constituents during the temperature increase.

To better understand the shrinkage behavior of our metamaterials and confirm the previous deduction, we also fabricated a single diamond element with $\theta_0 = 75^\circ$, $L_0 = 31.7$ mm and $H_0 = 10.2$ mm as seen in Fig. 4(a) to investigate its thermal response. We find that the elastomer beam deforms from straight to buckling when the sample was taken from the 3d printing tray in Fig. 4(b). It is concluded that the photochemical expansion emerges in the elastomer beam during the 3D printing process. At room temperature, the modulus of the glassy polymer is almost three orders of magnitude as that of the elastomer. Therefore, the outer ligaments of glassy polymer limit the expansion of the middle beam with the elastomer. It is noted that the photochemical expansion rate surpasses the critical value of compressively buckling in the elastomer beam. Compared with the elastomer beam diamond element with $\theta_0 = 75^\circ$ in Fig. 4(a), the elastomer beams in Fig. 3(a) are similarly compressed due to the photochemical expansion, however, their compressive strains do not exceed the critical buckling value. Fig. 4(c) shows the post heat-induced deformation of the structure at the temperature of 62.4 °C. When the temperature increases from 22.4 °C to 62.4 °C, the modulus of the glassy polymer decreases gradually to the near value as that of an elastomer after glass-transition

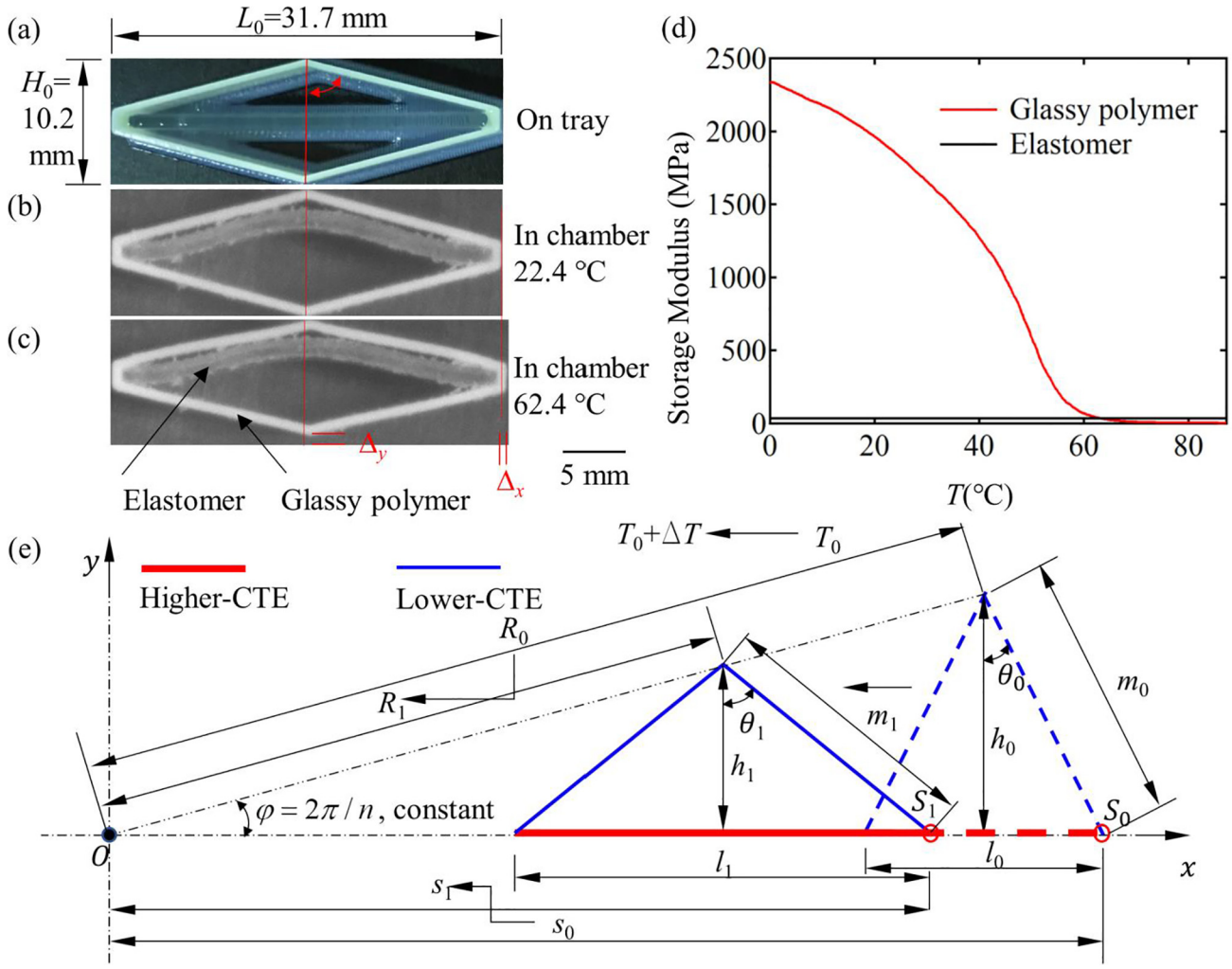

Fig. 4. Deformation mechanism of the planar unit cell under thermal load. (a) The diamond-shape element pasted on the tray of the printer, and (b) striped from the tray and placed in the chamber at room temperature. (c) Thermal deformation of a diamond element heated at a temperature of 62.4 °C. When the temperature rises from 22.4 °C to 62.4 °C, the Δ_x and Δ_y are found, which means that the elongation of the buckling beam causes to flatten the entire diamond-shaped element. (d) Young's modulus evolution with the increase of temperature of two constituents. (e) Inward movement of half diamond with the increase of temperature.

temperature (Fig. 4(d)). Meanwhile, the residual compressive strain/stress deposited in the elastomer is continuously released, expanding the elastomer beam with a horizontal increment of Δ_x and producing a vertical increment of Δ_y for the diamond which can be seen in Fig. 4(c). Yet, the elastomer beam does not completely stretch to the straight state, because of the strength mismatch of the two constituent materials. The comparison between Fig. 4(a) and (b) presents the existence of the photochemical expansion in 3D printing. The evolution of Fig. 4(b) to Fig. 4(c) demonstrates the heat-shrinkage in the planar unit cell with $\theta_0 = 60^\circ$.

Here on the tray in Fig. 4(a), the initial length of elastomer beam, L_0, is 31.7 mm and the initial height, H_0 10.2 mm. And the measured value Δ_x is 0.5 mm, and Δ_y −1.2 mm. After that, the transverse and perpendicular strain of the diamond can be calculated as $\varepsilon_x = 1.4\%$ and $\varepsilon_y = -11.6\%$. Here, the entire photochemical expansion of the elastomer beam includes the buckling and the post heat-induced deformation.

In order to calculate the entire photochemical expansion strain, the buckling beam in Fig. 4(b) and (c) can be regarded approximately as the sinusoidally curved ones. So, their shapes can be described as $y = h_0 \sin(\pi x/2L_0)$, where h_0 is the wave amplitude. Its length is given by

$$t = \int_0^{L_0} \sqrt{1 + (y')^2}\, dx = \int_0^{L_0} \sqrt{1 + \left[\frac{\pi h_0}{2L_0} \cos\left(\frac{\pi x}{2L_0}\right)\right]^2}\, dx \tag{1}$$

The obtained lengths of the buckling beam in the room temperature (Fig. 4(b) and 62.4 °C (Fig. 4(c)) are 32.4 mm and 32.9 mm, respectively. The elongation rate at room temperature is calculated as **2.2%**, while the one in 62.4 °C is **3.8%**. Logically, after removed from the tray and placed at room temperature, the elastomer beam is still constrained by the glassy polymer rhombus. It is observed that 2.2% is the only one part of the entire photochemical expansion strain of the elastomer beam in the buckling state in Fig. 4(b), and the other of that is still stored inside the beam as built-in compressive strain. While the modulus of the glassy polymer decreases in response to the temperature rise, the elastomer beam continues to expand until at **3.8%**.

An unusual phenomenon is shown that elastomer beam's photochameical expansion rate exceeds the critical buckling value. According to buckling equation, the critical load of buckling beam [32–35] is given as

$$P_{cr} = a\frac{\pi^2 EI}{l^2} \tag{2}$$

where I is the moment of inertia of a beam and a is a factor that depends on boundary conditions. $a = 4$ for clamped–clamped beams. As for rectangular section of the beam, the critical stress is expressed as

$$\sigma_{cr} = a\frac{\pi^2 E}{12(l/w)^2} \tag{3}$$

where w is the height of the beam and the corresponding critical compressive strain is

$$\varepsilon_{cr} = a\frac{\pi^2}{12(l/w)^2} \tag{4}$$

where l/w is the slenderness ratio of the rectangular beam, $w = 1.25$ mm. Substituting the specific values of the elastomer beam in the diamond with $\theta_0 = 75^\circ$, $l_0 = 31.7$ mm and $h_0 = 10.2$ mm, we obtain the critical buckling strain as $\varepsilon_{cr,75^\circ} = 0.5\%$, which is lower than 2.2% of the elongation rate in the elastomer beam in $\theta = 75^\circ$ (Fig. 4(b)). Meanwhile, due to $L_0 = 14.75$ mm in the diamond of the unit cell with $\theta_0 = 60^\circ$, $R_0 = 10$ mm and $n = 32$ in Fig. 3, the critical buckling strain is $\varepsilon_{cr,60^\circ} = 2.4\%$, which is higher than 2.2% of the elongation rate in the elastomer beam in $\theta_0 = 60^\circ$ (Fig. 3(a)). This is the reason why it is in the diamond with $\theta_0 = 75^\circ$ in Fig. 4(a) that the elastomer beams buckle rather than in the planar unit cell with $\theta_0 = 60^\circ$ in Fig. 3(a).

In Fig. 4(e), due to Δ_y, the circumference of the ring shortens. As a result, all the diamonds along the center O move inward with vertex sliding on the axis OG and elastomer sliding on the axis Ox, which is also proved by the comparison between Fig. 4(e) and A2(c) (Appendix). This law explains why the elastomer beams' photochemical expansion induces the shrinkage of the whole planar unit cell.

Regardless of the diamond element with $\theta_0 = 60^\circ$, $R_0 = 10$ mm and $n = 32$ in Fig. 3 or with $\theta_0 = 75^\circ$ and $R_0 = 10$ mm in Fig. 4(a), the deformation of the elastomer beam overcomes the influence from the thermal expansion coefficient (TEC) of the elastomer and the glassy polymer when the temperature increases. So, the photochemical expansion of the elastomer beam plays a more important role on the metamaterials than their TECs.

Irreversible heat-shrinkage

To show further irreversible heat-shrinkage of the planar unit cell in Fig. 3, we controlled the chamber temperature as increase–decrease cycles from ① to ⑦ as shown in Fig. 5(a), indicating that only heat-shrinkage from ① to ② happens, while other occasions belong to positive thermal expansion. Furthermore, the strain of 3% from ① to ② is far greater than the others, 0.5%. It is concluded that shrinkage from ① to ② derives from the irreversible photochemical expansion of the elastomer. On the other hand, the thermal strain of others results from the TEC of two constituents, which is the elastic and recoverable strain.

Theoretical predictions

To further validate the experiment results, direct stiffness method based on beams system [36,37] is used to solve the theoretical results. According to the central symmetry, the planar unit cell can be simplified as the triangular frame with boundary conditions described as Node 3 sliding on the Axis OG without rotation and Node 1, 2 sliding on Axis Ox without rotation as shown in Fig. 4(e) and A2(c) in Appendix. The residual compressive strain under critical buckling value, which is stored in middle elastomer beams, will be released gradually as the specimen is slowly heated from 22.4 °C to 62.4 °C. The specimen is transformed into a permanent shape, rather than elastic, recoverable one. So, here the heat-shrinkable strain shown in Fig. 5(b) ①–② is only regarded as the strain considering the strength degradation with the increase of temperature. The elastic thermal strain shown in Fig. 5(b) ②–⑦ is excluded.

The distance between the center and the outer endpoint S changes into $s_1 = s_0 + u_1$, where u_1 is the horizontal displacement of the outer point S_0. And the strain of the entire unit cell is described isotopically as $\varepsilon = \frac{s - s_0}{s_0}$. Substituting it to $\alpha = \frac{\varepsilon}{\Delta T}$, we can obtain the effective TEC as

$$\alpha = \frac{u_1}{\Delta T s_0} \tag{5}$$

where u_1 is the key factor which solves α. The solution of u_1 depends on the displacement solution of the triangular frame.

The triangular frame can be solved by the displacement method in structural mechanics using beam element [36,37] in Fig. A2(a). Based on assembling global stiffness matrix and thermal load, a 9×9 symmetric positive linear equations are produced as $[K]\{u\} = \{P\}$, where the details of $[K]$ and $[P]$ are listed as Appendix (a7) and (a8). Dealing with constraint conditions, we obtain a solution about $\{u_1 \ \ u_2 \ \ u_3\}^{\mathrm{T}}$, which is defined as a solution of a symmetric positive 3×3 linear equations $[K']\{u\} = \{P'\}$ or

$$\begin{bmatrix} K'_{11} & K'_{12} & K'_{13} \\ K'_{21} & K'_{22} & K'_{23} \\ K'_{31} & K'_{32} & K'_{33} \end{bmatrix} \begin{Bmatrix} u_1 \\ u_2 \\ u_3 \end{Bmatrix} = \begin{Bmatrix} P'_1 \\ P'_2 \\ P'_3 \end{Bmatrix} \tag{6}$$

where individual items in $[K']$ and $\{P'\}$ are given by

$$K'_{11} = \frac{A_h E_h}{l_0} + \frac{A_l E_l}{m_0}\sin^2\theta_0 + \frac{12E_l I_l}{m_0^3}\cos^2\theta_0 \tag{7}$$

$$K'_{12} = K'_{21} = -\frac{A_h E_h}{l_0} \tag{8}$$

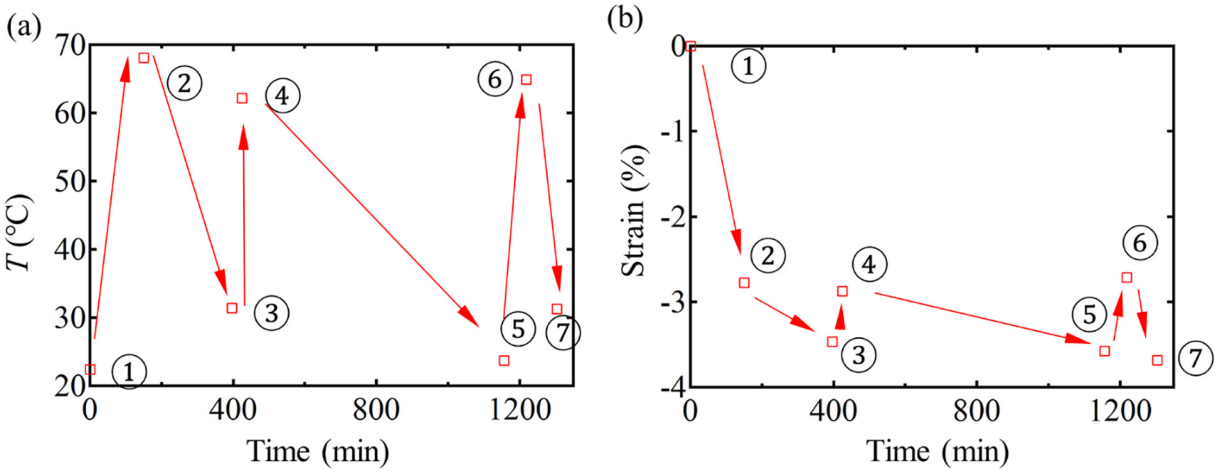

Fig. 5. The irreversible shrinkage of a planar unit cell. (a) Evolution of temperature and (b) the strain evolution with time.

$$K'_{13} = K'_{31} = -\frac{A_l E_l}{m_0}\sin^2\theta_0 - \frac{12E_l I_l}{m_0^3}\cos^2\theta_0 - \tan\phi\left(\frac{12E_l I_l}{m_0^3} - \frac{A_l E_l}{m_0}\right)\sin\theta_0\cos\theta_0 \quad (9)$$

$$K'_{22} = \frac{A_h E_h}{l_0} + \frac{A_l E_l}{m_0}\sin^2\theta_0 + \frac{12E_l I_l}{m_0^3}\cos^2\theta_0 \quad (10)$$

$$K'_{23} = K'_{32} = -\frac{A_l E_l}{m_0}\sin^2\theta_0 - \frac{12E_l I_l}{m_0^3}\cos^2\theta_0 + \tan\phi\left(\frac{12E_l I_l}{m_0^3} - \frac{A_l E_l}{m_0}\right)\sin\theta_0\cos\theta_0 \quad (11)$$

$$K'_{33} = 2\left(\frac{A_l E_l}{m_0}\sin^2\theta_0 + \frac{12E_l I_l}{m_0^3}\cos^2\theta_0\right) + 2\tan^2\phi\left(\frac{A_l E_l}{m_0}\cos^2\theta_0 + \frac{12E_l I_l}{m_0^3}\sin^2\theta_0\right) \quad (12)$$

where A_h, E_h, I_h, and l_0 represent the sectional area, the Young's Modulus, inertia moment and length of the elastomer beams, while A_l, E_l, I_l, and m_0 represent the sectional area, the Young's Modulus, inertia moment and length of the glassy polymer beams in Fig. 4(e) and Fig. A2. When the residual compressive strain, $\{\varepsilon_r\}$ stored in the elastomer beam is only considered, $\{P'\}$ is given as

$$\{P'\} = \begin{Bmatrix} E_h A_h \varepsilon_r \\ -E_h A_h \varepsilon_r \\ 0 \end{Bmatrix} \quad (13)$$

When the thermal load is only considered, $\{P'\}$ is given as

$$\{P'\} = \begin{Bmatrix} E_h A_h \alpha_h \Delta T + E_l A_l \alpha_l \Delta T \sin\theta \\ -E_h A_h \alpha_h \Delta T - E_l A_l \alpha_l \Delta T \sin\theta \\ 2E_l A_l \alpha_l \Delta T \cos\theta \tan\phi \end{Bmatrix} \quad (14)$$

where E_h, A_h, I_h, l_0 stand for Young's Modulus, sectional area, moment inertia and length of the elastomer beam, E_l, A_l, I_l, m_0 the ones of the glassy polymer. More details on solution process of Eq. (6) are listed in Literature [36].

Eq. (6) is an implicit expression about the 3 × 3 linear equations system. The *LU* Decomposition Method is adopted to solve it using FORTRAN [36]. In Fig. 6 we report theoretically the evolution of the thermal and heat-shrinkable strain with the increase of the temperature respectively, which agree with the experimental results at the temperature of 68.1 °C in the thermal strain. The thermal strain in Fig. 6(b), elastic recoverable, is corresponding to Fig. 5(b) ②–⑦, while the heat-shrinkable strain in Fig. 6(c), unrecoverable, results from gradually released photochemical expansion and is equivalent to Fig. 5(b) ①–②. But in the heat-shrinkable strain, the experimental value is lower than the analytical, which indicates that the elastomer beams produce creep deformation and partial residual stress disappears in the process of the temperature rise.

Optimization

To find a maximum value of heat-shrinkable strain in the proposed metamaterials, we developed a parametric optimization scheme, whereas the input parameters are taken to be the photochemical expansion strain of the elastomer ε_r, the half vertex angle θ, the angle φ. Note that to ensure the convergence in the calculation, we limited in every optimization problem a fixed range of every input parameter. The optimization problem was solved using Composite Shape Algorithm (CSA) [38], which is an effective solution for nonlinearly constrained optimization problems with low dimensionality. For each evaluation of the objective function, a numerical simulation using the analytical model was conducted to derive the heat-shrinkable strain ε for the set of input ε_r, θ, and φ determined by CSA. Note that the input parameters were constrained as $\varepsilon_r \in [0.1\%,5\%]$, $\theta \in [30^\circ,75^\circ]$, and to make sure that the resulting configuration was always well defined. In Fig. 7 we report why the photochemical expansion strain is taken as [0.1%,5%].

According to Eq. (2), we can calculate three photochemical expansion strains as 0.1%, 3.1% and 4.7% including 28-min, 62-min and 116-min printing time in Fig. 7(a)–(c). So, experimental results show that photochemical expansion rate also rises with the increase of layer printing time and nozzle proceeding direction. If this maximum value of photochemical expansion strain, 5%, is stored in the middle beams and their slenderness ratio is lower than the critical value, this built-in compressive strain will be released totally while the temperature approaches *Tg* (glassy transition temperature) of the glassy polymers. According to the analytical model, the entire unit cell will shrink 7.5% when the photochemical expansion strain is taken as 5%. In order to obtain the more heat-shrinkable rate of the proposed metamaterials, we need to extend the layer printing time and make nozzle proceeding direction perpendicular to the beam direction.

Considering the critical buckling of the elastomer beam shown in Eq. (4), we introduce another constraint as

$$\varepsilon_r < \varepsilon_{cr} = a\frac{\pi^2}{12(l/w)^2} \quad (15)$$

According to Fig. 4(e) and R0 = 10 mm, the length of the elastomer beam l_0 is given as $l_0 = 2R_0\tan\theta_0\sin\varphi$. The Eq. (5) transfers into

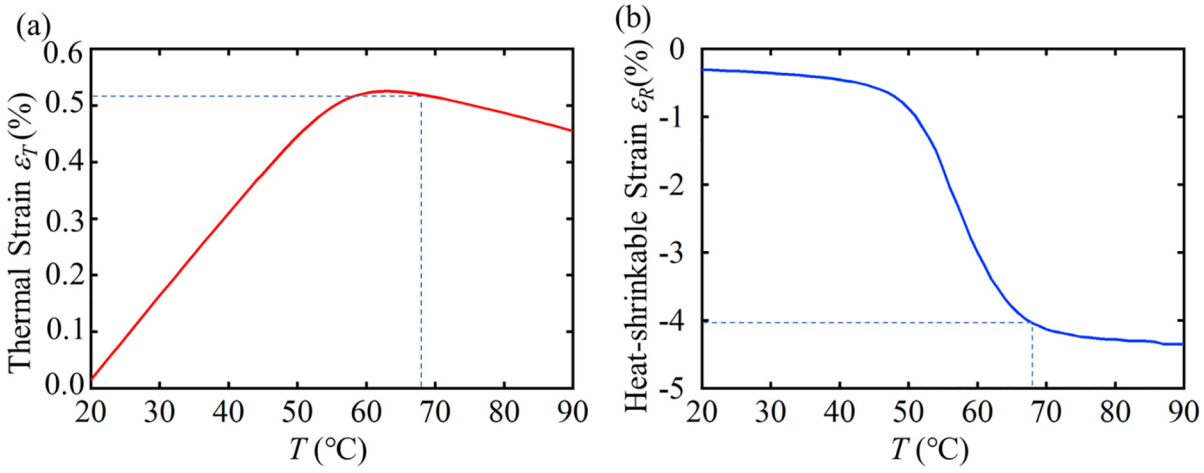

Fig. 6. Thermal (elastic recoverable (a), corresponding to Fig. 5(b) ②-⑦) and heat-shrinkable (unrecoverable (b), corresponding to Fig. 5(b) ①-②) strain as a function of temperature. Note that the temperature on the transverse axis is meaning the thermal load from 22.4 °C to the current one.

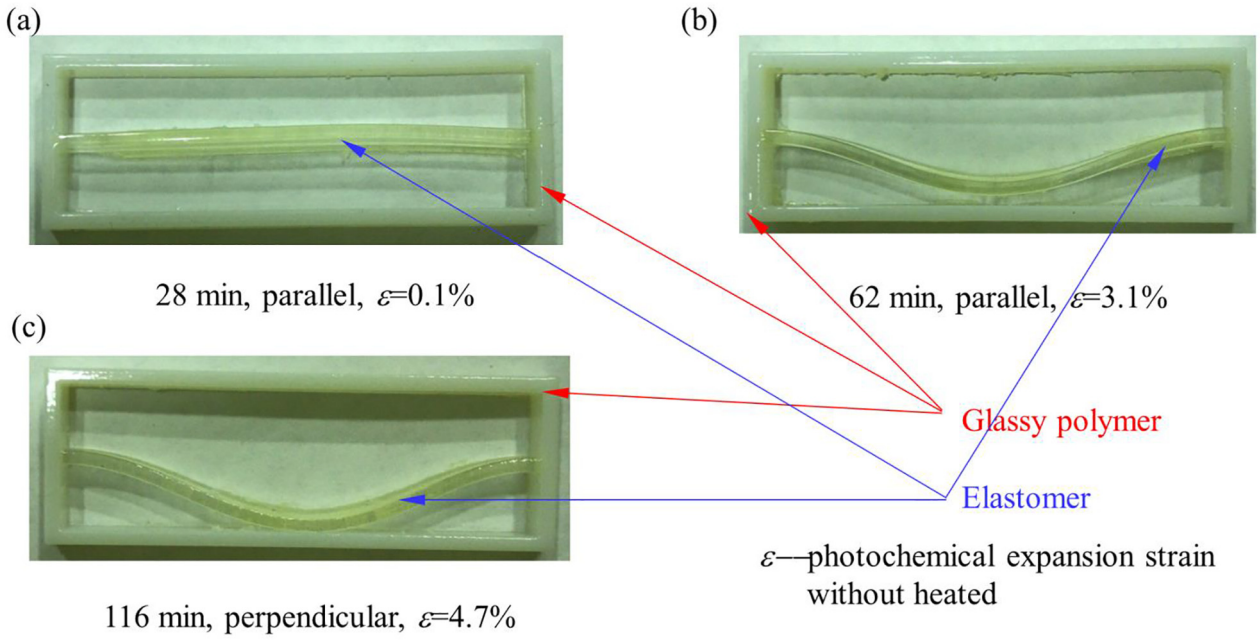

Fig. 7. The photochemical expansion strain rises with the increase of layer printing time and a nozzle moving direction. (a) The sample's printing time is 28 min and longer beams are parallel to nozzle proceeding direction, and (b) The sample's printing time is 62 mins and parallel each other, and (c) The sample's printing time 116 min and perpendicular.

$$\varepsilon_r < \varepsilon_{cr} = \frac{a\pi^2 w^2}{12(2R_0 \tan\theta_0 \sin\varphi)^2} \tag{16}$$

According to Fig. 4(e), and Eqs. (1), (6), and (13), the heat-shrinkable strain is expressed as

$$\varepsilon = \frac{u_1}{R(\cos\varphi + \tan\theta_0 \sin\varphi)} \tag{17}$$

which is a function $\varepsilon(\varepsilon_r, \theta_0, \varphi)$ about photochemical expansion strain ε_r, the half vertex angle θ_0, and the angle φ.

To this end, we minimized the heat-shrinkable strain with $\varepsilon_r \in [0.1\%, 5\%]$, $\theta_0 \in [30^\circ, 75^\circ]$, $\varepsilon_r < \varepsilon_{cr}$, $\varphi = \pi/12$, $\pi/16$, or $\pi/20$, and combined Eqs. (6)–(13). After 23 iterations the algorithm finds the maximum value of the heat-shrinkable strain, 8.3%, for $\varepsilon_r = 5\%$, $\theta_0 = 68.1^\circ$. Simulation validation as shown in Fig. A3 shows that 5% of photochemical expansion in planar unit cell with $\theta_0 = 68.1^\circ$ does cause the 8.3% heat-shrinkable strain.

Conclusions

In summary, we have proposed an approach to create heat-shrinkable metamaterials by 3D printing with a permanent shrinkage rate of −2.8% to −8.3%. Through the experiments, we have shown that the photochemical expansion occurs in the elastomer beam after fabrication. As the vertex angle of the diamond increases, the slenderness ratio of the beam turns greater. Until beyond the critical value, the elastomer beam becomes buckling. As the strength in the glassy polymer weakens with the temperature rise, the limitation upon the elastomer beam will relax, which induces positive transverse strain and negative vertical strain in the diamond. Consequently, the unit cell shrinks isotropically and permanently due to the evenly central arrangement and a good agreement between the experiment and analytical prediction were observed. The experiments show that by tuning layer printing time and nozzle proceeding direction, heat-shrinkable strain turns greater. The findings presented here can be extended to 3D and tubular metamaterials, paving an avenue to design heat shrinkage materials with potential applications in aerospace, coating, protection industries, microrobotics, biomedical devices, and biomimetic systems. The proposed design also can facilitate the creation of gradually evolving non-uniform or more complex structures via thermal stimuli, such as 4D printing.

Acknowledgements

Y. Li gratefully acknowledges the financial support from the China Scholarship Council (File No. 201508420188). The authors thank Dr. Yanyu Chen at NREL for reading through the whole manuscript and giving insightful comments and suggestions. The authors gratefully acknowledge the National Science Foundation (CMMI-1462270), the Region 2 University Transportation Research Center (UTRC), and the Office of Naval Research.

A. Appendix

By following the Standard Test Method in ASTM D696-03, the coefficient of linear thermal expansion of glassy polymer and elastomer were gauged as $1.64 \times 10^{-4}\,^\circ\mathrm{C}^{-1}$ and $3.0 \times 10^{-4}\,^\circ\mathrm{C}^{-1}$ within the range from 25 °C to 100 °C, using the 3D printed prismatic test specimens with 6 mm × 6 mm × 100 mm. This result is consistent with the literature [22].

Nodal forces and moments are denoted as $\{U_i \;\; V_i \;\; M_i\}^{\mathrm{T}}$, and $\left\{U_j \;\; V_j \;\; M_j\right\}^{\mathrm{T}}$, and nodal displacements and rotations as $\{u_i \;\; v_i \;\; \varphi_i\}^{\mathrm{T}}$, and $\{u_j \;\; v_j \;\; \varphi_j\}^{\mathrm{T}}$ at Node i and j in a beam element on the local coordinate system. In three beam elements of the global coordinate system in Fig. A2(c), Beam I is made of Node 2 and 1, Beam II Node 2 and 3, Beam III Node 3 and 1. The element local stiffness matrix is conducted as

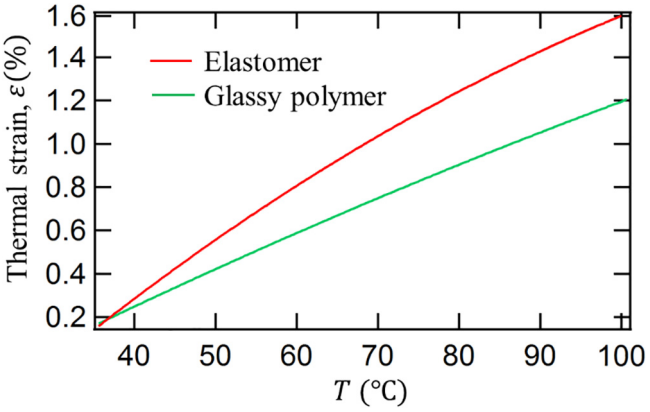

Fig. A1. The strain-temperature curve of elastomer and glassy polymer.

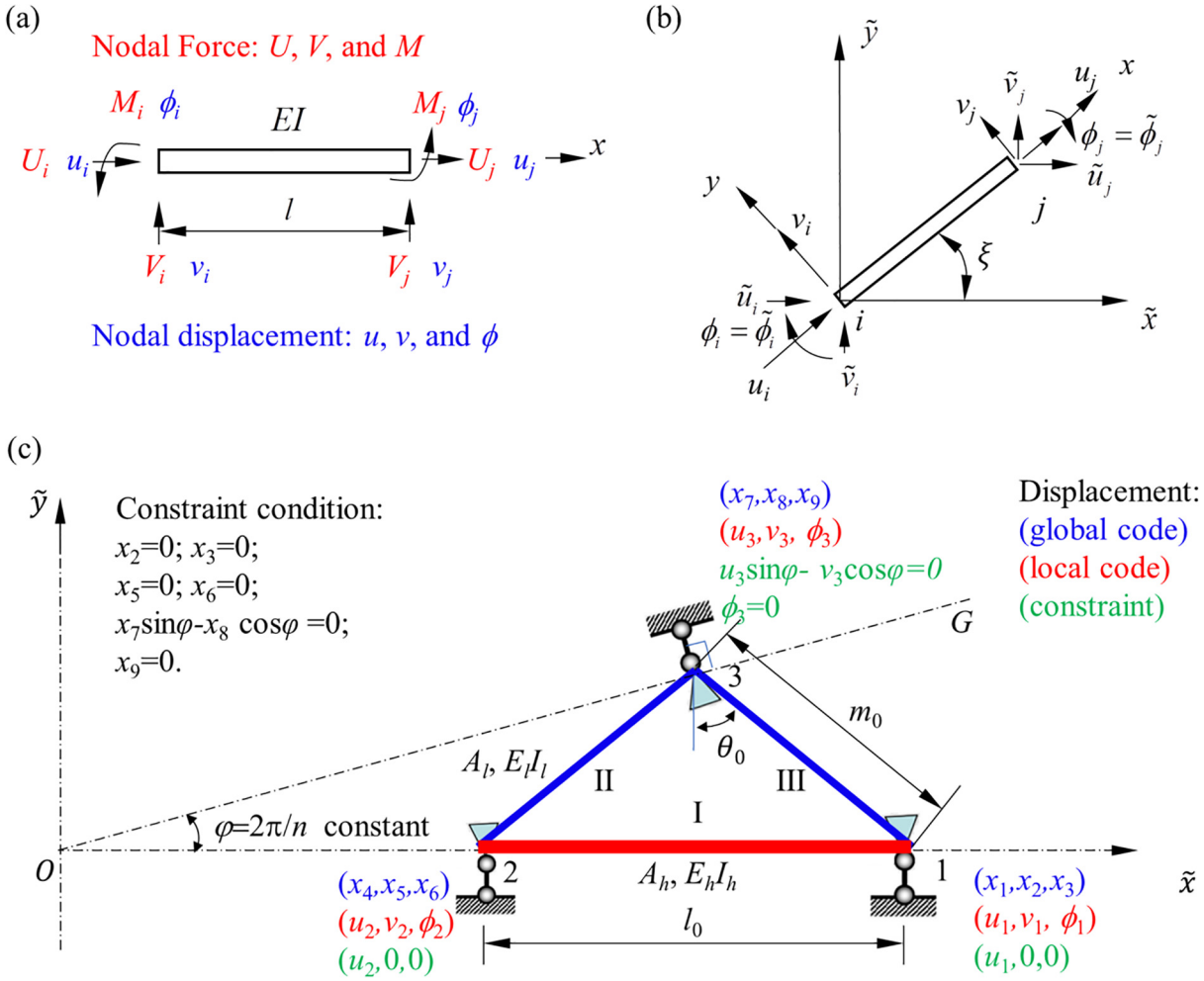

Fig. A2. Beam element and triangular rigid frame with boundary conditions. (a) Beam element with nodal displacements, rotations, forces, and moments. (b) Conversion from the local system to the global system. (c) Elements, nodes, and constraint conditions.

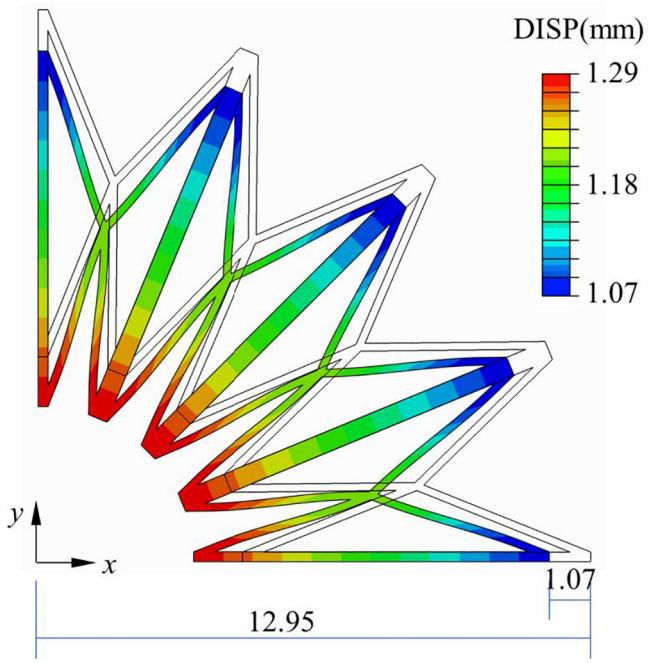

Fig. A3. The deformation contour indicates the displacement field of the planar unit cell with $w_e = 0.2$ mm, $w_g = 0.5$ mm, $\theta_0 = 68.1^\circ$, $R_0 = 10$ mm, and $n = 32$ when the photochemical expansion (5%) in the middle elastomer beams is only considered.

$$[k]^e = \begin{bmatrix} \frac{AE}{l} & 0 & 0 & -\frac{AE}{l} & 0 & 0 \\ 0 & \frac{12EI}{l^3} & \frac{6EI}{l^2} & 0 & \frac{-12EI}{l^3} & \frac{6EI}{l^2} \\ 0 & \frac{6EI}{l^2} & \frac{4EI}{l} & 0 & \frac{-6EI}{l^2} & \frac{2EI}{l} \\ -\frac{AE}{l} & 0 & 0 & \frac{AE}{l} & 0 & 0 \\ 0 & \frac{-12EI}{l^3} & \frac{-6EI}{l^2} & 0 & \frac{12EI}{l^3} & \frac{-6EI}{l^2} \\ 0 & \frac{6EI}{l^2} & \frac{2EI}{l} & 0 & \frac{-6EI}{l^2} & \frac{4EI}{l} \end{bmatrix} \tag{A.1}$$

where A, E, I, l denote the sectional area, Young's Modulus, inertia moment and length of a beam element.

References

[1] Kong D, Xiao X. Rigid high temperature heat-shrinkable polyimide tubes with functionality as reducer couplings. Sci Rep 2017:7.
[2] Xiao X, et al. Shape-memory polymers with adjustable high glass transition temperatures. Macromolecules 2015;48(11):3582–9.
[3] Wang Q, et al. Lightweight mechanical metamaterials with tunable negative thermal expansion. Phys Rev Lett 2016;117(17):175901.
[4] Boatti E, Vasios N, Bertoldi K. Origami metamaterials for tunable thermal expansion. Adv Mater 2017.
[5] Ai L, Gao XL. Metamaterials with negative Poisson's ratio and non-positive thermal expansion. Compos Struct 2017;162:70–84.
[6] Xu H, Farag A, Pasini D. Multilevel hierarchy in bi-material lattices with high specific stiffness and unbounded thermal expansion. Acta Mater 2017.
[7] Vaia R, Baur J. Adaptive composites. Science 2008;319(5862):420–1.
[8] Campbell, D, et al. Development of a Shape Memory Coilable Boom Using Elastic Memory Composite Material. in Biennial Conference on Engineering, Construction, and Operations in Challenging Environments. 2014.
[9] Hu J. Preparation of shape memory polymers – shape memory polymers and textiles – 2. Shape Memory Polymers & Textiles 2007:28–61.
[10] Behl M, Razzaq MY, Lendlein A. Multifunctional shape-memory polymers. Adv Mater 2010;22(31):3388–410.
[11] Xu K, Chen Y. Photocuring temperature study for curl distortion control in projection-based stereolithography. J Manuf Sci Eng 2017;139(2):021002.
[12] Liravi F, Das S, Zhou C. Separation force analysis and prediction based on cohesive element model for constrained-surface stereolithography processes. Comput Aided Des 2015;69:134–42.
[13] DebRoy T, et al. Building digital twins of 3D printing machines. Scr Mater 2017;135:119–24.
[14] Yang Q, et al. Finite element modeling and validation of thermomechanical behavior of Ti-6Al-4V in directed energy deposition additive manufacturing. Addit Manuf 2016;12:169–77.
[15] Fergani O, et al. Analytical modelling of residual stress in additive manufacturing. Fatigue Fract Eng Mater Struct 2017;40(6):971–8.
[16] Yangbo L, Dahai H, Jianshu O. Fast algorithms of the simulation analysis of the thermal stresses on concrete dams during construction periods. Phys Proc 2012;24:1171–7.
[17] Zhu B. Thermal stress and temperature control in massive concrete. Power Publisher of China; 1999.
[18] Gladman AS, et al. Biomimetic 4D printing. Nat Mater 2016;15(4):413–8.
[19] Choong YYC, et al. 4D printing of high performance shape memory polymer using stereolithography. Mater Des 2017;126:219–25.
[20] Naficy S, et al. 4D printing of reversible shape morphing hydrogel structures. Macromol Mater Eng 2017:302(1).
[21] Zarek M, et al. 4D Printing of Shape Memory-Based Personalized Endoluminal Medical Devices. Macromol Rapid Commun 2017;38(2).
[22] Ding Z, et al. Direct 4D printing via active composite materials. Sci Adv 2017;3(4):e1602890.
[23] Zarek M, et al. 3D printing of shape memory polymers for flexible electronic devices. Adv Mater 2016;28(22):4449–54.
[24] Rafsanjani A, et al. Hydro-responsive curling of the resurrection plant Selaginella lepidophylla. Sci Rep 2015:5.
[25] Brulé V, et al. Hierarchies of plant stiffness. Plant Sci 2016;250:79–96.
[26] Bauhofer AA, et al. Harnessing Photochemical Shrinkage in Direct Laser Writing for Shape Morphing of Polymer Sheets. Adv Mater 2017.
[27] Jager EW, Inganäs O, Lundström I. Microrobots for micrometer-size objects in aqueous media: potential tools for single-cell manipulation. Science 2000;288(5475):2335–8.
[28] Lendlein A, Langer R. Biodegradable, elastic shape-memory polymers for potential biomedical applications. Science 2002;296(5573):1673.
[29] Zakharchenko S, et al. Stimuli-responsive hierarchically self-assembled 3D porous polymer-based structures with aligned pores. J Mater Chem B 2013;1(13):1786–93.
[30] Karalekas D, et al. Investigation of shrinkage-induced stresses in stereolithography photo-curable resins. Exp Mech 2002;42(4):439–44.
[31] Karalekas D, Aggelopoulos A. Study of shrinkage strains in a stereolithography

cured acrylic photopolymer resin. J Mater Proc Tech 2003;136(1):146–50.
[32] Wang L, Ortiz C, Boyce MC. Mechanics of Indentation into Micro- and Nanoscale Forests of Tubes, Rods, or Pillars. J Eng Mater Technol 2011;133(1):011014.
[33] Fu H, et al. Morphable 3D mesostructures and microelectronic devices by multistable buckling mechanics. Nat Mater 2018;17(3):268–76.
[34] Mosadegh B, et al. Pneumatic networks for soft robotics that actuate rapidly. Adv Funct Mater 2014;24(15):2163–70.
[35] Yang D, et al. Buckling of elastomeric beams enables actuation of soft machines. Adv Mater 2015;27(41):6323–7.
[36] Li Y, et al. Hoberman-sphere-inspired lattice metamaterials with tunable negative thermal expansion. Compos Struct 2018.
[37] Wei K, et al. Tailorable thermal expansion of lightweight and robust dual-constituent triangular lattice material. J Appl Mech 2017;84(10):101006.
[38] Yaoqing W. Collection of Programming Code in Optimization Method. Beijing: Workers Publisher; 1983.